**Supporting Information**

# Interfacial Engineering of $FeWO_4/Fe_2O_3$ Homometallic Heterojunction for Synergistic Electrocatalytic Water Splitting

Rongfang Li,[a] Heng Zhang,[a,b*] Junling Chen[c], Ka Zhang[a,b], Wenqiang Li[a], Xun Feng,[a,*] Huijuan Zhang,[a] Abdoulkader Ibro Douka,[d*] Xu Zhang,[d] Tiexin Zhang[d,*]

[a.] College of Chemistry and Chemical Engineering, Luoyang Normal University, Luoyang, 471934, P. R. China

[b.] College of Chemistry, Zhengzhou University, Zhengzhou, 450001, P. R. China

[c.] School of Biochemistry and Chemical Engineering, Nanyang Institute of Technology, Nanyang, 473601, P. R. China

[d.] State Key Laboratory of Fine Chemicals, School of Chemical Engineering, School of Chemistry, Dalian University of Technology, Dalian 116024, P. R. China

*Corresponding authors E-mail:

hnzhangheng95@163.com

fengx@lynu.edu.cn

akimdouka@dlut.edu.cn

zhangtiexin@dlut.edu.cn

## Chemicals and materials

Ferric chloride hexahydrate ($FeCl_3 \cdot 6H_2O$), Sodium tungstate dihydrate($Na_2WO_4 \cdot 2H_2O$) potassium hydroxide (KOH), hydrofuloric acid (HF) and hydrochloric acid (HCl) were purchased from Aladdin Ltd (Shanghai, China). Commercial $IrO_2$ and Pt/C was purchased from Sigma-Aldrich. Nafion solution (5 wt%) provided by Dupont China Holding Co., Ltd (Tianjin, China). Ni Foam with a thickness of 1.6 mm and 120 ppi (pore per square inch) was purchased from Jia Shide Foam Metal Co., Ltd (Suzhou, China). Deionized water was used throughout the experiments.

## Material characterizations

The morphology of nanoparticles was observed by SEM (Hitachi S4800). All samples for the TEM analysis prepared by depositing a drop of the diluted suspension in ethanol on carbon film-coated copper grid. The high-resolution transmission electron microscopy (HRTEM, JEM-2010FEF) was conducted on an FEI TECNAI F20 microscope at an acceleration voltage of 200 kV. The crystal phase of all synthesized materials was determined by powder XRD using a PANalytical Empyrean, Netherlands X-ray diffractometer with Cu Kα radiation source. X-Pay photoelectron spectroscopy (XPS) measurements were performed with a VG Scientific ESCALAB 210 electron spectrometer using Mg KR radiation under a vacuum of $2\times10^{-8}$ Pa at 14 KV.

## Electrochemical measurements

All electrochemical measurements were performed in a conventional three-electrode system at room temperature using a CHI 660E electrochemical analyzer (CHI Instruments, Shanghai, China). A platinum wire was used as counter electrode for OER and a graphite road for HER. The reference electrode employed for all measurement was a saturated calomel electrode (SCE). The synthesized catalysts with a geometric area of 1 $cm^{-2}$ were directly served as the working electrodes. For powdery catalysts, the working electrodes were prepared by dropping catalyst ink onto nickel foam with a load of 1 mg $cm^{-2}$. The inks were obtained by sonicating the mixture containing catalysts, 5 mg of catalyst ($FeWO_4/Fe_2O_3$,$Fe_2O_3$, Pt/C and $IrO_2$), 475 μL of ethanol, 475 μL of water and 50 μL of 5 wt % Nafion for 30 min. The ink mix is applied to nickel foam in a load of 1 mg $cm^{-2}$. The 1 M KOH aqueous solution was used as the electrolytes, and all the polarization curves were recorded at a scan rate of 5 mV $s^{-1}$ unless specifically indicated. In HER and OER characterizations, the polarization curves were iR-corrected using the equation: $E_{iR\text{-}corrected}$ = E-iR, where E is the original potential, R is the solution resistance, i is the corresponding current, and $E_{iR\text{-}corrected}$ is the iR-corrected potential. Polarization curves of all samples for HER and OER with 100% iR-compensation.

Electrochemical impedance spectroscopy (EIS) tests were carried out in a frequency ranging from 0.1 Hz to 100 kHz with AC amplitude of 10 mV. Furthermore, the HER and OER potentials were converted to RHE scale according to the equation: E(vs. RHE) = E (vs. SCE) + 0.059*pH +0.241 V, where the pH value of 13.969 for 1 M KOH.

## ECSA calculation

Electrochemical capacitance measurements were used to determine the active surface area of each catalyst. To estimate the electrochemical active surface area of the electrocatalysts, double-layer capacitance ($C_{dl}$) was considered in the non-faradaic region (-0.654 ~ -0.714 V vs. RHE) of CVs recorded at different scan rates of 20, 40, 60, 80, 120 and 140 mV $s^{-1}$. Then, plotting the double-layer charging current at -0.684 V vs. scan rate yields a linear slope, which is equivalent to twice the value of $C_{dl}$. Finally, the ECSA was obtained through dividing $C_{dl}$ by the specific capacitance of electrode material. Generally, the specific capacitance for flat surface electrodes is 0.06 mF $cm^{-2}$.

## Turnover frequency calculations

To calculate the per-site turnover frequency (TOF), we used the following formula according to previous reports[1].

$$TOF\ per\ site = \frac{\#Total\ Hydrogen\ Turn\ Overs/cm^2\ geometric\ area}{\#\ Surface\ Sites/cm^2\ geometricarea}$$

The number of total hydrogen turn overs is calculated from the current density using the following equation:

$$\#H_2 = \left(j\frac{mA}{cm^2}\right)\left(\frac{1Cs^{-1}}{1000mA}\right)\left(\frac{1\ mol\ e^{-1}}{96485.3C}\right)\left(\frac{1\ mol\ H_2}{2\ mol\ e^{-1}}\right)\left(\frac{6.022\times10^{23}\ H_2\ molecules}{1\ mol\ H_2}\right)$$

$$= 3.12\times10^{15}\frac{H_2/s}{cm^2}per\frac{mA}{cm^2}$$

The total number of effective surface sites was calculated based on the following equation:

$$\frac{\#Surfacesites}{cm^2\ geometric\ area} = \frac{\#Surfacesites(flat\ standard)}{cm^2\ geometric\ area}\times Roughness\ factor$$

Here the roughness factor (Rf) can be determined by the double-layer capacitance ($C_{dl}$). The surface sites of $2\times10^{15}$ for the flat standard electrode was used for our calculation according to previous results.[1] Thus, the number of surface active sites for the $Ni_2P$@NC/NF catalyst is estimated to be: $(3.95 \times 10^3/60) \times 2 \times 10^{15}$ surface sites/$cm^2$ = $1.31 \times 10^{17}$ surface sites/$cm^2$.

Therefore, in 1 M KOH solution, the TOF per site for the $Ni_2P$@NC/NF catalyst at $\eta_{100}$ is calculated as follows:

$$(3.12 \times 10^{15} \frac{H_2/s}{cm^2} / \frac{mA}{cm^2})(45.6 \frac{mA}{cm^2})(\frac{1\ cm^2}{6.63 \times 10^{17}}) = 1.09\ H_2/s$$

**Theoretical calculation.**

The Density Functional Theory (DFT) calculations were carried out using the Castep module of Materials Studio. The electron exchange and correlation interactions were described by adopting the generalized gradient approximation (GGA) method with the Perdew-Burke-Ernzerhof (PBE) functional, and the interactions between core electrons and valence electrons were described by projector augmented-wave (PAW) method. The Monkhorst-Pack grid k-points of 3×3×1 were adopted to integrate the Brillouin zone, and the kinetic cut-off energy was set at 400 eV. The convergence thresholds for energy and force were set at $1.0\times10^{-5}$ eV/atom and 0.02 eV $Å^{-1}$, respectively. The self-consistence field (SCF) tolerance was set to $1.0\times10^{-5}$ eV/atom. To calculate the hydrogen adsorption energy, we constructed the theoretical models of $FeWO_4$, $Fe_2O_3$ and $FeWO_4$,/$Fe_2O_3$ heterostructure with the vacuum space of 15 Å. The calculations for both $FeWO_4$ and $Fe_2O_3$ were conducted on (100) and (001) crystal plane according to the literatures, respectively.[2] Then, the heterostructure model was constructed by adjusting the arrangement of the two

surfaces. The Gibbs free energies of hydrogen adsorption ($\Delta G_{H^*}$) were calculated as follow:

$$\Delta G_{H^*} = \Delta E_{H^*} + \Delta E_{ZPE} - T\Delta S$$

Where $\Delta E_{H^*} = E_{(slab+H^*)} - E_{(slab)} - E_{H2}/2$, $\Delta E_{ZPE}$ stands for the change in zero-point energy and $\Delta S$ represents the entropy change.[3] Norskov et al. previously reported that $\Delta E_{ZPE} - T\Delta S$ is approximately 0.24 eV.[4] Therefore, we take $\Delta G_{H^*} = \Delta E_{H^*} + 0.24$ eV.

The four sequential electron transfer steps, including adsorption steps (i and iii), dissociation steps (ii and iv) and desorption step (v). Considering that the overall water decomposition process requires energy 4.92 eV at the standard conditions, the energy for at least one step in (i–iv) should be larger or equal to 1.23 eV. For the OER in alkaline environment, the whole process occurs via the following four elementary steps:

$$OH^- + * \rightarrow OH^* + e^- \quad (1)$$

$$OH^* + OH^- \rightarrow O^* + H_2O + e^- \quad (2)$$

$$O^* + OH^- \rightarrow OOH^* + e^- \quad (3)$$

$$OOH^* + OH^- \rightarrow O_2 + H_2O + e^- \quad (4)$$

The adsorption free energies ($\Delta G$) of OER intermediates can be obtained by $\Delta Gi = \Delta Ei + \Delta ZPEi - T\Delta Si$, where i means OH*, O* and OOH*. Li et al. previously reported that $\Delta ZPE - T\Delta S$ are 0.06, 0.37 and 0.44 eV for O*, OH* and OOH*, respectively.[5] Furthermore, the $\Delta E$ for OER intermediates was calculated as follow:

$$\Delta E_{OH} = E(OH^*) - E(^*) - [E(H_2O) - 1/2E(H_2)]$$

$$\Delta E_{O} = E(O^*) - E(^*) - [E(H_2O) - E(H_2)]$$

$$\Delta E_{OOH} = E(OOH^*) - E(^*) - [2E(H_2O) - 3/2E(H_2)]$$

Therefore, the Gibbs free energy changes for the four elementary steps of OER can be expressed as follows:

$$\Delta G_1 = \Delta G_{OH} - eU$$

$$\Delta G_2 = \Delta G_{O} - \Delta G_{OH} - eU$$

$$\Delta G_3 = \Delta G_{OOH} - \Delta G_{O} - eU$$

$$\Delta G_4 = 4.92\ eV - \Delta G_{OOH} - eU$$

Where U is the potential measured against the normal hydrogen electrode (NHE) at standard conditions. Therefore, the theoretical overpotential ( $\eta$ ) for OER can be obtained by the following equation:

$$\eta_{OER} = \max[\Delta G_1, \Delta G_2, \Delta G_3, \Delta G_4]/e - 1.23\ [V]$$

# Figure

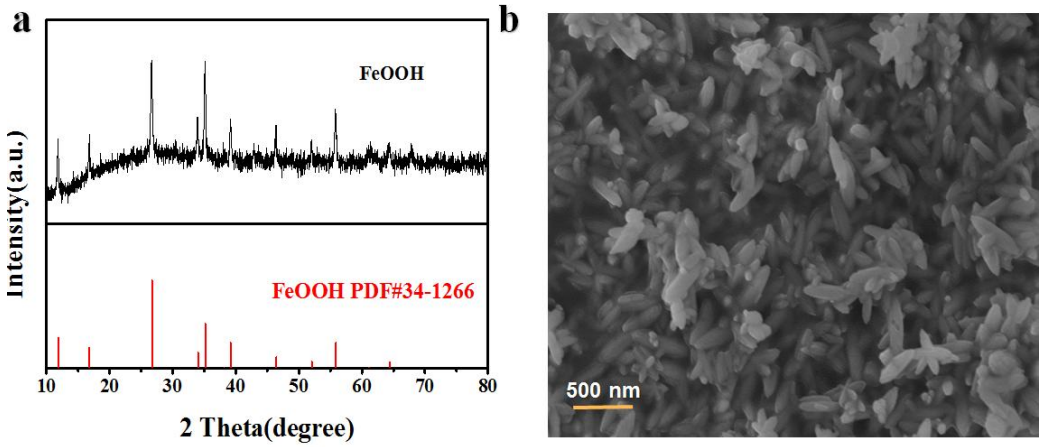


Fig. S1. (a) XRD pattern and (b)SEM image of FeOOH hybrid.

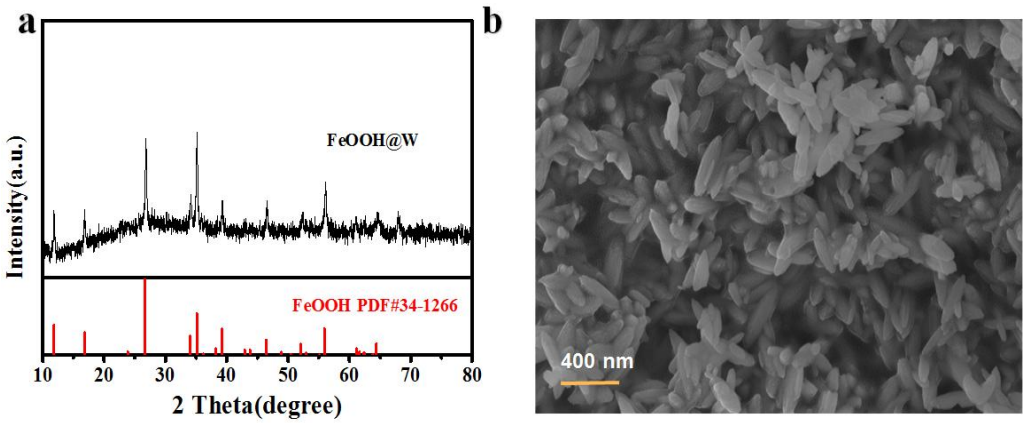


Fig. S2. (a) XRD pattern and (b) SEM image of FeOOH@W complex hybrid.

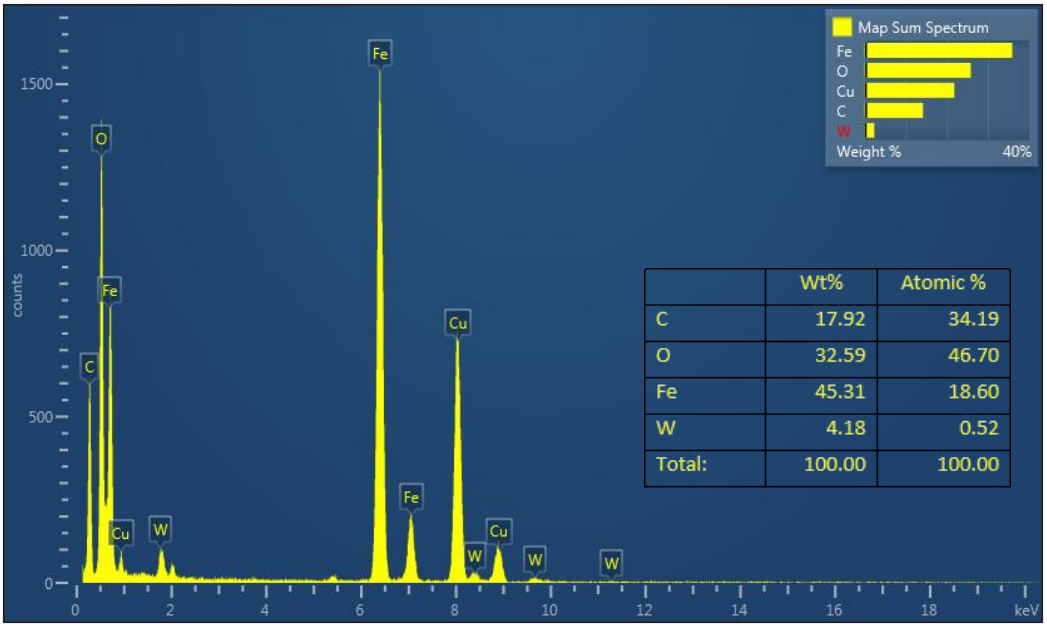


| | Wt% | Atomic % |
|---|---|---|
| C | 17.92 | 34.19 |
| O | 32.59 | 46.70 |
| Fe | 45.31 | 18.60 |
| W | 4.18 | 0.52 |
| Total: | 100.00 | 100.00 |

Fig. S3. EDS spectrum of the $FeWO_4/Fe_2O_3$.

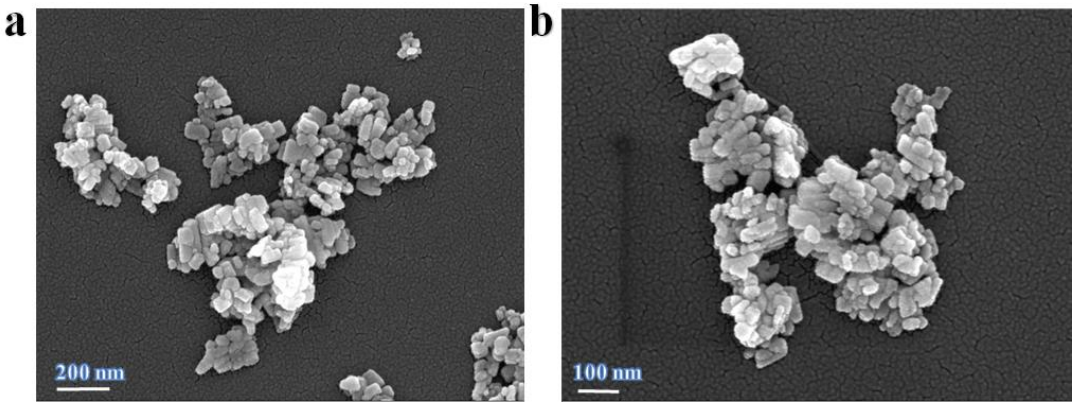


Fig. S4. SEM image of $Fe_2O_3$ at different magnifications.

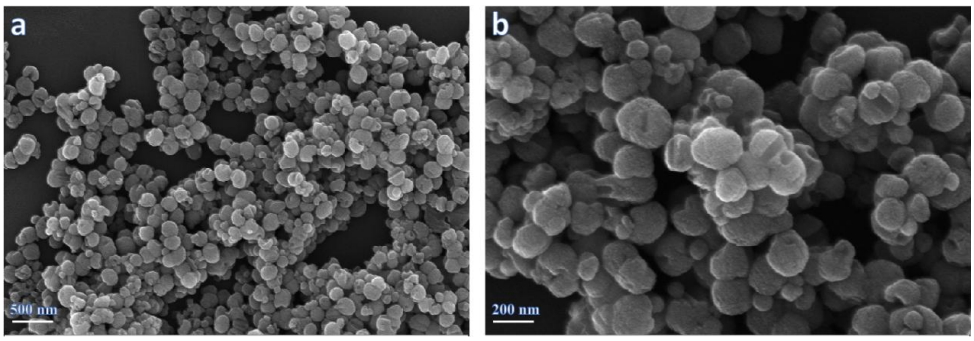


Fig. S5. SEM image of $Fe_2O_3$ at different magnifications.

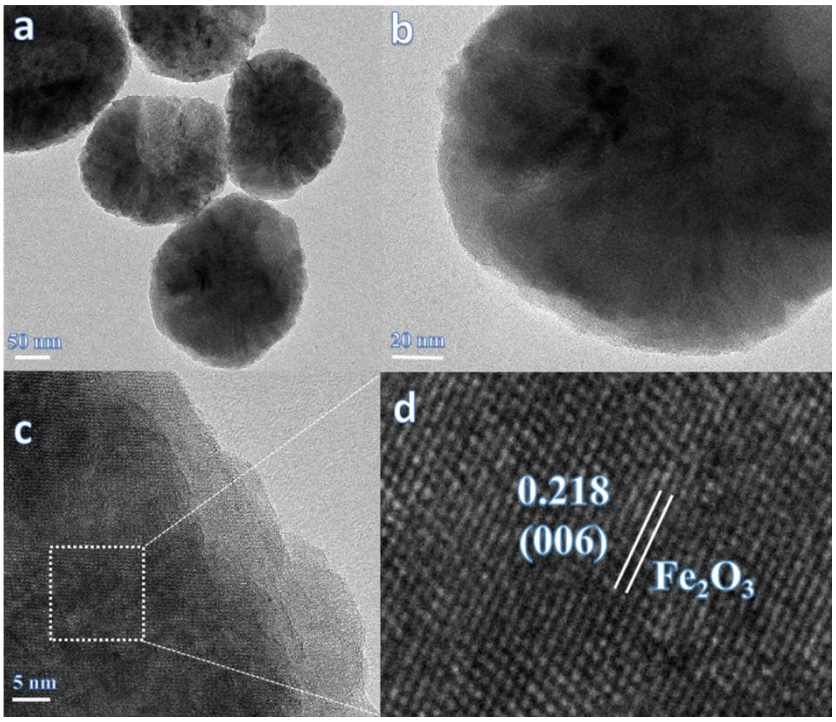


Fig. S6. (a-b) HRTEM image image of $Fe_2O_3$. (d) Enlarged portion of the white box in the Fig. c.

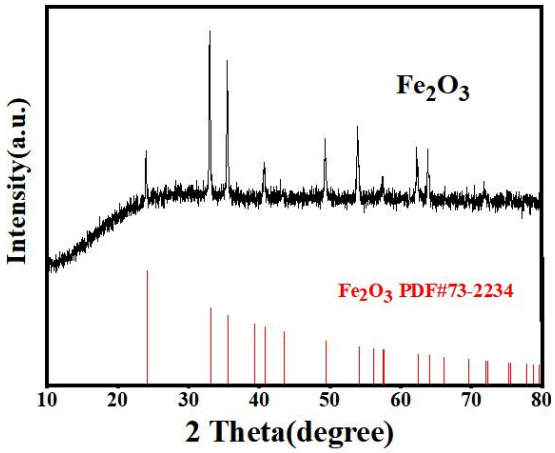


Fig. S7. XRD pattern of $Fe_2O_3$.

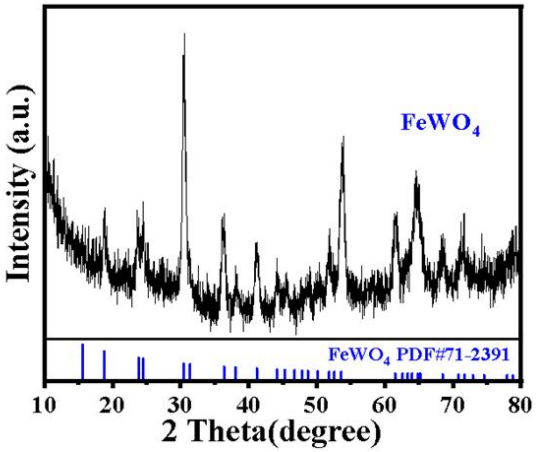


Fig. S8. (a) XRD pattern of $FeWO_4$.

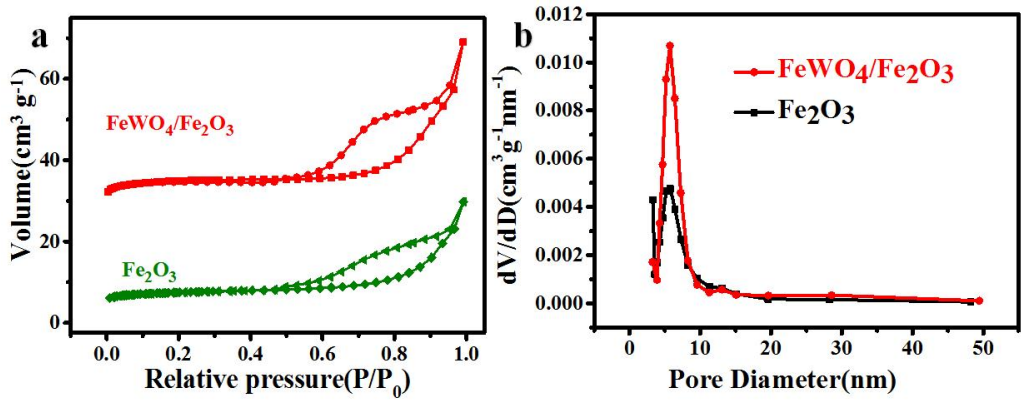


Fig. S9. (a) Nitrogen adsorption-desorption isotherms (b) the pore size distribution curves of the $FeWO_4/Fe_2O_3$ and $Fe_2O_3$.

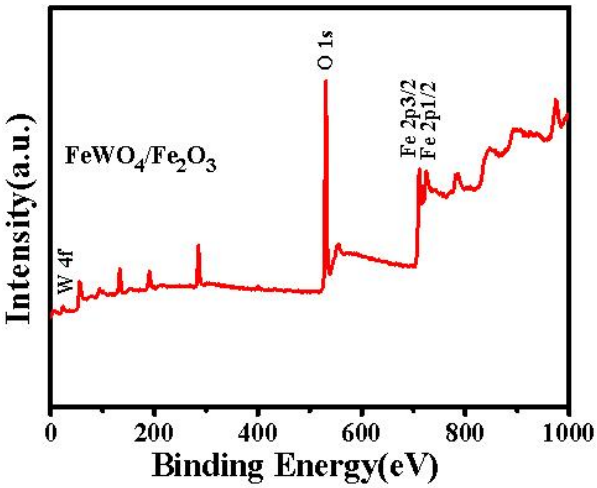


Fig. S10. XPS spectra of $FeWO_4/Fe_2O_3$.

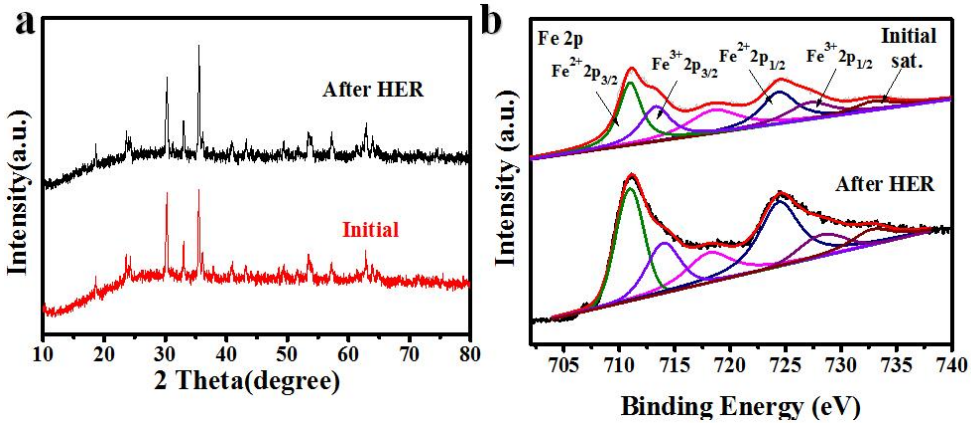


Fig. S11. (a) XRD pattern and (b) XPS spectra of $FeWO_4/Fe_2O_3$ of Fe 2p after HER durability test.

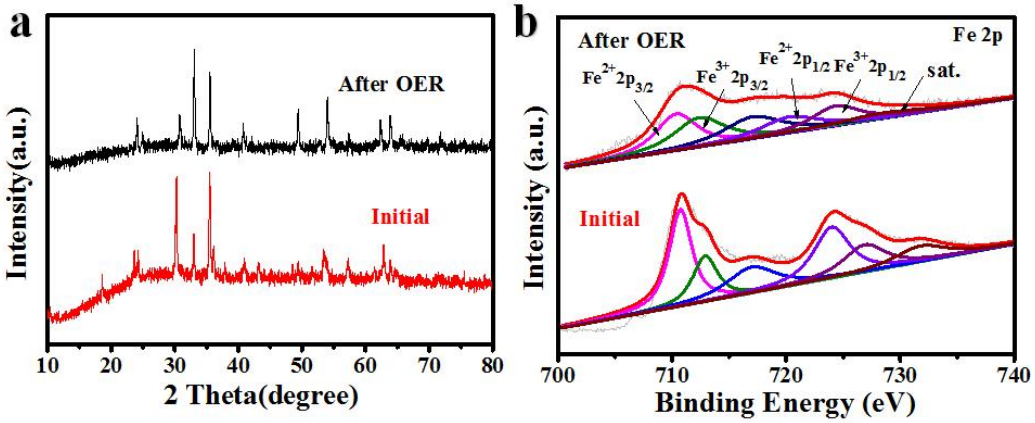


Fig. S12. (a) XRD pattern and (b) XPS spectra of $FeWO_4/Fe_2O_3$ of Fe 2p after long time OER durability test.

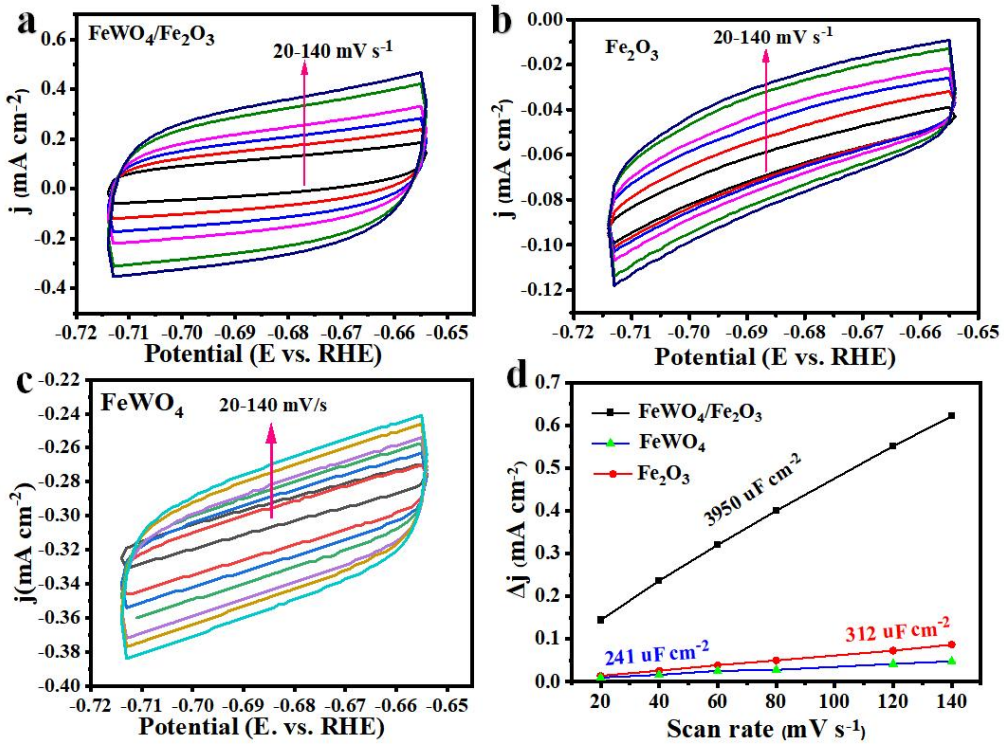


Fig. S13. Cyclic voltammogram (CV) curves at different scan rates for (a) $FeWO_4/Fe_2O_3$, (b) $Fe_2O_3$, (c) $FeWO_4$, (d) The current density variation at 0.389 V versus RHE plotted against the scan rates.

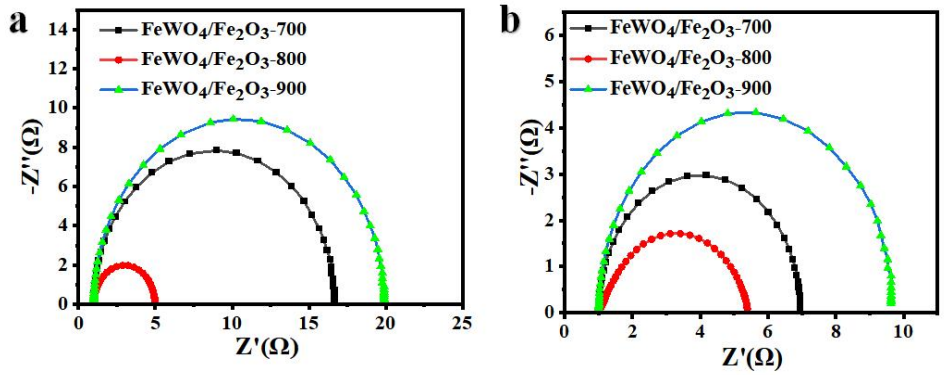


Fig. S14. Nyquist plots of $FeWO_4/Fe_2O_3$-700 and $FeWO_4/Fe_2O_3$-900 measured for HER at overpotential of 150 mV (A) and (B) for OER at overpotential of 350 mV.

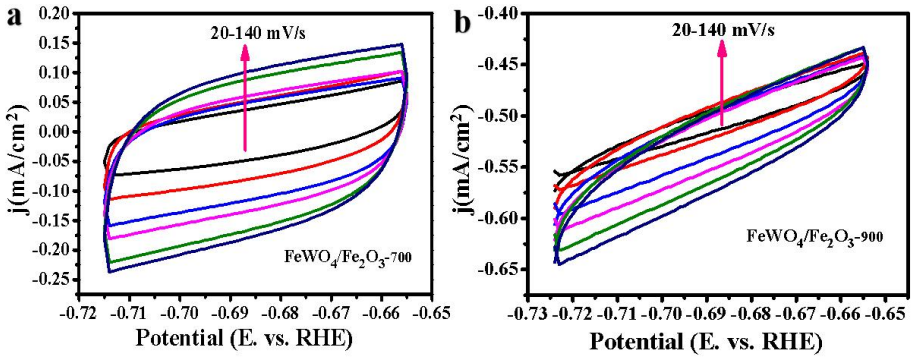


Fig. S15. Cyclic voltammogram (CV) curves at different scan rates for (A) $FeWO_4/Fe_2O_3$-700 and (B) $FeWO_4/Fe_2O_3$-900.

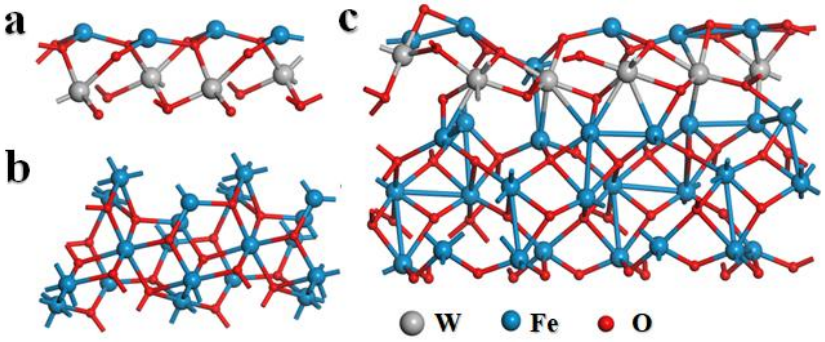


Fig. S16. Theoretical structure models of $FeWO_4$ (100) surface, $Fe_2O_3$ (001) surface and $FeWO_4/Fe_2O_3$ interface.

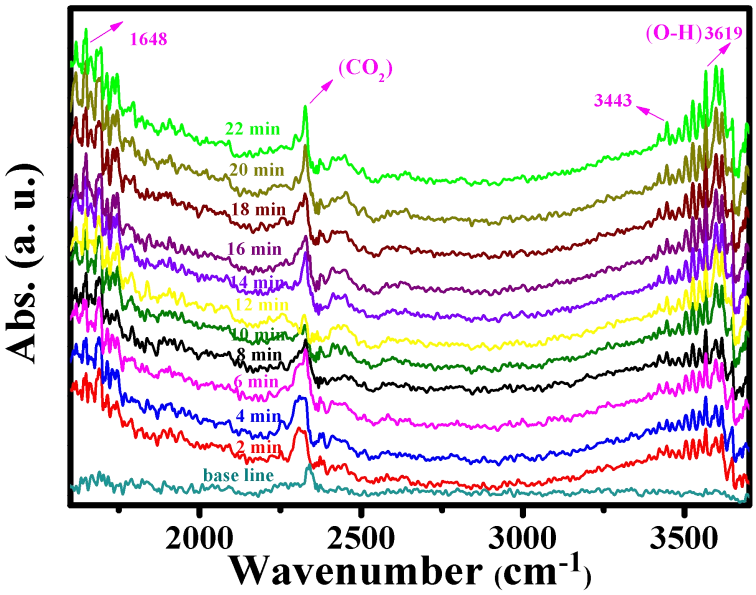


Fig. S17. *In situ* FTIR of $FeWO_4/Fe_2O_3$ at a overpotential of 350 mV in 1 M KOH.

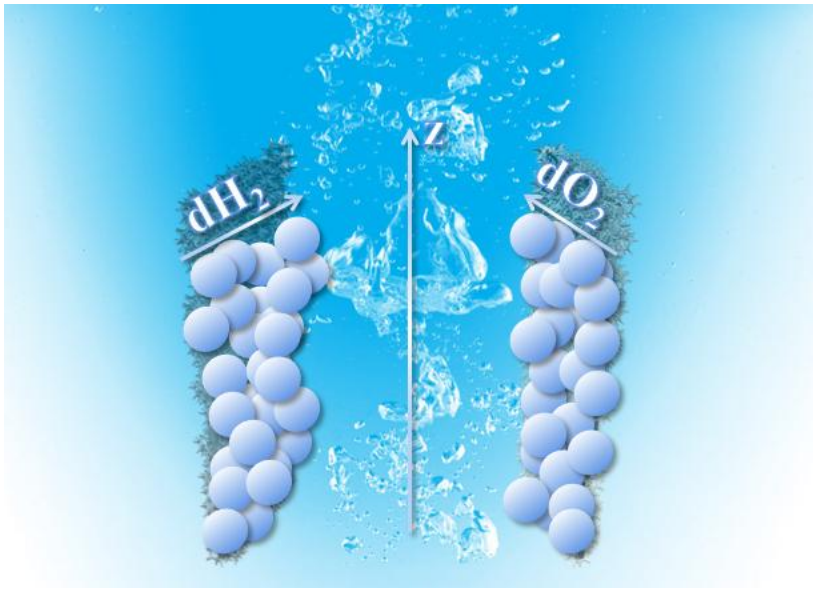


Fig. S18. Schematic representation of the separation of hydrogen and oxygen bubbles from the surface during water splitting

During the water electrolysis, hydrogen and oxygen gases are formed on the surface of the electrodes, and they can only be separated from the surface upon reaching sufficient size. The coverage of the electrode surface by the formed bubbles can increase the total resistance of the system, resulting in a reduction of the interface between the electrode and the electrolyte. Therefore, the accumulation of bubbles increases the amount of the overpotential required for electrolysis of water.

Before discussing the development of bubble separation strategies from the electrode surface, a careful study of the bubble behavior separation from the electrode surface during the water electrolysis reaction is required. In general, a bubble can be removed from the surface and penetrate the electrolyte when its diameter reaches a critical value [45,46]. Schematic represents the separation of hydrogen and oxygen bubbles is shown in Fig. above. The motion direction of the bubbles is along the x and z-axes. The motion in the x-direction is due to the difference in the concentration of gas bubbles in the electrolyte, whereas movement in the z-direction is due to the density difference between the gas bubble and the electrolyte. Therefore, the resultant force in the x and z-direction determines the direction of motion of the gas bubbles. If the bubble separation rate is low on the surface of the electrode, a layer of bubbles is formed on the surface, and its thickness will be a function of its height. As the schematic Fig. indicates, with increasing height, the thickness of this layer is also increased. The low separation rate of the bubbles will increase the effect of the bubble, which will increase the IR drop, consequently increasing the overpotential.

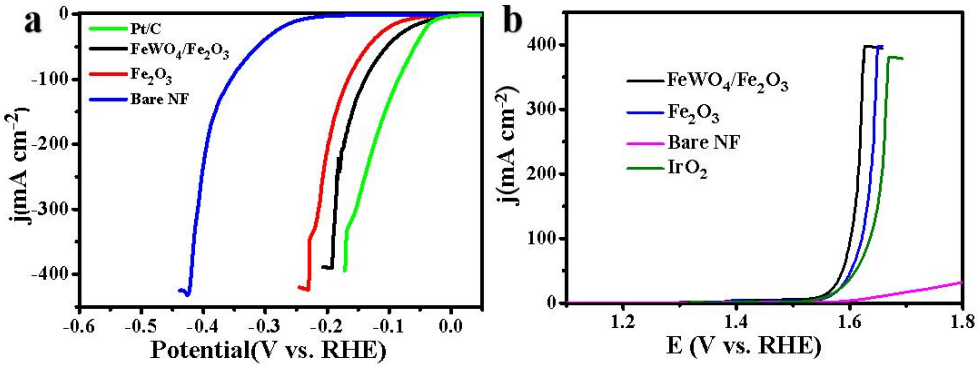


Fig. S19. The saturated performances of homometallic heterojunction $FeWO_4/Fe_2O_3$ and other control catalysts under high current densities in the electrocatalytic HER and OER, respectively.

when increasing the over-potentials, the working current densities of heterojunction $FeWO_4/Fe_2O_3$ reached the saturated platform statues at around 400 mA $cm^{-2}$ for HER and OER, respectively. Importantly, the similar saturated current densities were also observed in the cases of using control catalysts such as $Fe_2O_3$, bare NF, and $IrO_2$ when increasing the over-potentials. Those comprehensive results further implied that the saturation current densities were not only determined by the

nature of electrode materials, but also hugely affected by the kinetics of specific reaction conditions and experimental set ups.

Table S1 HER comparison in 1.0 M KOH with the recently reported literatures

| Materials | Tafel slope (mV $dec^{-1}$) | $\eta_{10}$ / mV | Reference |
|---|---|---|---|
| **$FeWO_4/Fe_2O_3$** | **63.3** | **38** | **This work** |
| $Ni_3N$-$V_2O_3$-3-1 | 50 | 57 | [6] |
| Co/MoN | 77.5 | 52 | [7] |
| 1T–$MoS_2$ QS/$Ni(OH)_2$ | 30 | 57 | [8] |
| NiMoN/$Ni_3N$-6 | 76 | 46 | [9] |
| (Ni, Fe)$S_2$@$MoS_2$ | 101.22 | 130 | [10] |
| $Ni(OH)_2/Ni_3S_2$ | 49 | 50 | [11] |
| $W_2N$/WC | 58.7 | 148.5 | [12] |
| $Fe_3O_4$-FeS/IF | 126.3 | $\eta_{20}$ 120.8 | [13] |
| MoP/$MoO_2$ | 41 | 79 | [14] |
| CoP/$Co_2P$ | 51.8 | 68 | [15] |
| P-$MoS_2$@CoP/CC | 51.2 | 64 | [16] |
| $FeNi_3$-$MoO_2$/NF | 60.1 | 50.8 | [17] |
| 1T-$MoS_2/CoS_2$ | 60 | 71 | [18] |
| $Ni_3S_2$@NiV-LDH/NF | 90 | 126 | [19] |

Table S2 OER comparison in 1.0 M KOH with the recently reported literatures

| Materials | Tafel slope (mV $dec^{-1}$) | j($mA/m^2$) | OER(mV) | Reference |
|---|---|---|---|---|
| **$FeWO_4/Fe_2O_3$** | **57** | **10** | **315** | **This work** |
| Fe-CoO/C | 60 | 10 | 362 | [20] |
| $Co_9S_8$@$MoS_2$ | 94 | 10 | 340 | [21] |
| $W_2N$/WC | 122.8 | 10 | 320 | [12] |
| $NiCo_2O_4$/NCNTs/NiCo | 89 | 10 | 350 | [22] |
| NiO/$NiCo_2O_4$ | 67 | 10 | 450 | [23] |
| $NiSe_2$/$CoSe_2$-T | 65 | 10 | 337 | [24] |
| CoO/$Co_xP$ | 101 | 10 | 370 | [25] |
| $Ni_3Se_4$/UCL-3 | 89.4 | 10 | 350 | [26] |
| CoO-$MoO_2$ | 69 | 10 | 312 | [27] |
| $Fe_2O_3$-MnO/NF | 66 | 10 | 370 | [28] |
| CoFe-Co@PNC | 81 | 10 | 320 | [29] |
| $NH_2$-MIL-88B(Fe) | 60 | 10 | 410 | [30] |
| NiCoP/C | 96 | 10 | 330 | [31] |
| CoCx/FeCo@C/rGO | 73.9 | 10 | 390 | [32] |

Table S3. at η = 100 mV, TOF of $FeWO_4/Fe_2O_3$, $Fe_2O_3$ and $FeWO_4$ in 1 M KOH solution.

| Colum TOF | HER | OER |
|---|---|---|
| **$FeWO_4/Fe_2O_3$** | 1.09 $s^{-1}$ | 0.2 $s^{-1}$ |
| **$Fe_2O_3$** | 0.56 $s^{-1}$ | 0.05 $s^{-1}$ |
| **$FeWO_4$** | 0.27 $s^{-1}$ | 0.03 $s^{-1}$ |

Table S4 Summary of overall water-splitting electrocatalysts

| Materials | **Overpotential (mV@10 mA/cm$^2$)** | Reference |
|---|---|---|
| **$FeWO_4/Fe_2O_3$** | **1.62** | **This work** |
| $mCo_{0.5}Fe_{0.5}P/rGO$ | 1.66 | [33] |
| $MoS_2$-$NiS_2$/NGF | 1.64 | [34] |
| NiS/Ni2P/CC | 1.62 | [35] |
| $Ni(OH)_2/Ni_3S_2$ | 1.64 | [11] |
| $CoCO_3$@NiFe LDH | 1.67 | [36] |
| $Fe_3O_4$-CoPx/TiN | 1.75 | [37] |
| CoFe@CNWs | 1.64 | [38] |
| Co-$Co_2C$/CC | 1.63 | [39] |
| $Co_2P$/CoN-in-NCNT | 1.64 | [40] |
| $Co_{0.8}Fe_{0.2}P$/NF | 1.67 | [41] |
| CoFeZr oxides/NF | 1.63 | [42] |
| CoP@FeCoP/NC | 1.68 | [43] |
| MoNi/$NiMoO_x$@NiFe | 1.64 | [44] |

## Reference


1. H. Zhang, W.Q. Li, X. Feng, L. Zhu, Q.Z. Fang, S. Li, L.Y. Wang, Z.J. Li and Z.K. Kou, A chainmail effect of ultrathin N-doped carbon shell on $Ni_2P$ nanorod arrays for efficient hydrogen evolution reaction catalysis, *J. Colloid. Interf. Sci.,* 2022, **607**, 281-289.

2. L.Y. Zeng, K.A. Sun, X.B. Wang, Y.Q. Liu, Y. Pan, Z. Liu, D.W. Cao, Y. Song, S.H. Liu and C.G. Liu, Three-dimensional-networked $Ni_2P/Ni_3S_2$ heteronanoflake arrays for highly enhanced electrochemical overall-water-splitting activity, Nano Energy, 2018, **51**, 26-36.

3. L.H. Ou, F. Yang, Y. Liu and S.L. Chen, First-principle study of the adsorption and dissociation of $O_2$ on Pt (111) in acidic media, J Physi. Chem. C, 2009, **113**, 20657-20665.

4. J.K. Nørskov, A. Logadottir, J. Kitchin, J.G. Chen, S. Pandelov and U. Stimming,

Trends in the exchange current for hydrogen evolution, *J Electrochem Soc.,* 2005, **152**, J23.
5. X.R. Gao, X.M Liu, W.J. Zang, H.L. Dong, Y.J. Pang, Z.K. Kou, P.Y. Wang, Z.H. Pan, S.R. Wei, S.C. Mu and J. Wang, Synergizing in-grown $Ni_3N$/Ni heterostructured core and ultrathin $Ni_3N$ surface shell enables self-adaptive surface reconfiguration and efficient oxygen evolution reaction, *Nano Energy,* 2020, **78**, 105355.
6. P. Zhou, G.Y. Zhai, X.S. Lv, Y.Y. Liu, Z.Y. Wang, P. Wang, Z.K. Zheng, H.F. Cheng, Y. Dai and B.B. Huang, Boosting the electrocatalytic HER performance of $Ni_3N$-$V_2O_3$ via the interface coupling effect, *Appl. Catal. B,* 2021, **283**, 119590.
7. J.W. Sun, W.J. Xu, C.X. Lv, L.J. Zhang, M. Shakouri, Y.H. Peng, Q.Q. Wang, X.F. Yang, D. Yuan, M.H. Huang, Y.F. Hu, D.J. Yang and L.X. Zhang, Co/MoN hetero-interface nanoflake array with enhanced water dissociation capability achieves the Pt-like hydrogen evolution catalytic performance, *Appl. Catal. B,* 2021, **286**, 119882.
8. W.S. Chen, J.J. Gu, Y.P. Du, F. Song, F.X. Bu, J.H. Li, Y. Yuan, R.C. Luo, Q.L. Liu and D. Zhang, Achieving rich and active alkaline hydrogen evolution heterostructures via interface engineering on 2D 1T-$MoS_2$ quantum sheets, *Adv. Funct. Mater.* 2020, **30**, 2000551.
9. W. Hua, H.H. Sun, H.Y. Liu, Y.Y. Li, J.-G. Wang, Interface engineered NiMoN/$Ni_3N$ heterostructures for enhanced alkaline hydrogen evolution reaction, *Appl. Surf. Sci.,* 2021, **540**, 148407.
10. Y.K. Liu, S. Jiang, S.J. Li, L. Zhou, Z.H. Li, J.M. Li and M.F. Shao, Interface engineering of (Ni, Fe)$S_2$@$MoS_2$ heterostructures for synergetic electrochemical water splitting, *Appl. Catal. B,* 2019, **247**, 107-114.
11. Q.H. Xu, H. Jiang, H.X. Zhang, Y.J. Hu, C.Z. Li, Heterogeneous interface engineered atomic configuration on ultrathin $Ni(OH)_2$/$Ni_3S_2$ nanoforests for efficient water splitting, *Appl. Catal. B,* 2019, **242**, 60-66.
12. J.X. Diao, Y. Qiu, S.Q. Liu, W.T. Wang, K. Chen, H.L. Li, W.Y. Yuan, Y.T. Qu, X.H. Guo, Interfacial engineering of $W_2N$/WC heterostructures derived from solid-state synthesis: a highly efficient trifunctional electrocatalyst for ORR, OER, and HER, *Adv. Mater.,* 2020, **32**, 1905679.
13. M. Yang, W.-H. Hu, M.-X. Li, Y.-N. Cao, B. Dong, Y. Ma, H.-Y. Zhao, F.-G. Wang, J. Huang and Y.-M. Chai, Controlled high-density interface engineering of $Fe_3O_4$-FeS nanoarray for efficient hydrogen evolution, J. Energy. Chem., 2022, **68**, 96-103.
14. M.M. Ding, H. Xu, M.X. Liu, Y.T. Wang, A.Q. Wang, T. Lin, L. Zhang and K. Zhang, Interface construction and porosity engineering to trigger efficient hydrogen evolution of two-dimensional porous molybdenum phosphide/dioxide heterojunction nanosheets in acidic and alkaline electrolytes, *Chem. Eng. J.,* 2020, **430**, 132674.
15. Y.P. Hua, Q.C. Xu, Y.J. Hu, H. Jiang and C.Z. Li, Interface-strengthened CoP nanosheet array with $Co_2P$ nanoparticles as efficient electrocatalysts for overall water splitting, *J. Energy. Chem.,* 2019, **37**, 1-6.
16. Y. Hu, H.B. Yu, L.L. Qi, J.X. Dong, P.X. Yan, T.T. Isimjan and X.L. Yang, Interface engineering of needle-like P-doped $MoS_2$/CoP arrays as highly active and

durable bifunctional electrocatalyst for overall water splitting, ChemSusChem, 2021, **14**, 1565-1573.
17. Q.L. Xu, T.Q. Yu, J.L. Chen, G.F. Qian, H.N. Song, L. Luo, Y.L. Chen, T.Y. Liu, Y.Z. Wang and S.B. Yin, Coupling interface constructions of $FeNi_3$-$MoO_2$ heterostructures for efficient urea oxidation and hydrogen evolution reaction, *ACS Appl. Mater. Inter.,* 2021, **13**, 16355-16363.
18. Y.Y. Feng, T. Zhang, J.H. Zhang, H. Fan, C. He and J.X. Song, 3D 1T-$MoS_2$/$CoS_2$ heterostructure via interface engineering for ultrafast hydrogen evolution reaction, Small, 2020, **16**, 2002850.
19. Q.Q. Liu, J.F. Huang, Y.J. Zhao, L.Y. Cao, K. Li, N. Zhang, D. Yang, L. Feng and L.L. Feng, Tuning the coupling interface of ultrathin $Ni_3S_2$@ NiV-LDH heterogeneous nanosheet electrocatalysts for improved overall water splitting, Nanoscale, 2019, **11**, 8855-8863.
20. W.M. Li, M.X. Li, C. Wang, Y. Wei and X.F. Lu, Fe doped CoO/C nanofibers towards efficient oxygen evolution reaction, *Appl. Surf. Sci.,* 2020, **506**, 144680.
21. J.M. Bai, T. Meng, D.L. Guo, S.G. Wang, B.G. Mao, M.H. Cao, $Co_9S_8$@$MoS_2$ core-shell heterostructures as trifunctional electrocatalysts for overall water splitting and Zn-air batteries, *ACS Appl. Mater. Inter.,* 2018, **10**, 1678-1689.
22. C. Chen, H. Su, L.-N. Lu,Y.-S. Hong, Y. Chen, K. Xiao, T. Ouyang, Y.L. Qin, Z.-Q. Liu, Interfacing spinel $NiCo_2O_4$ and NiCo alloy derived N-doped carbon nanotubes for enhanced oxygen electrocatalysis, *Chem. Eng. J.,* 2021, **408**, 127814.
23. R. Mondal, H.S. Ratnawat, S. Kumar, A. Kumar, P. Singh, Ni stabilized rock-salt structured CoO; $Co_{1-x}Ni_xO$: tuning of electrons to develop a novel OER catalyst, *RSC Adv.,* 2020, **10**, 17845-17853.
24. X.R. Zheng, X.P. Han, Y.H. Cao, Y. Zhang, D. Nordlund, J.H. Wang, S.L. Chou, H. Liu, L.L. Li, C. Zhong, Y.D. Deng and W.B. Hu, Identifying dense $NiSe_2$/$CoSe_2$ heterointerfaces coupled with surface high-valence bimetallic sites for synergistically enhanced oxygen electrocatalysis, *Adv. Mater.,* 2020, **32**, 2000607.
25. Y. Niu, M.L. Xiao, J.B. Zhu, T.T. Zeng, J.D. Li, W.Y. Zhang, D. Su, A.P. Yu, Z.W. Chen, A "trimurti" heterostructured hybrid with an intimate CoO/$Co_xP$ interface as a robust bifunctional air electrode for rechargeable Zn-air batteries, *J. Mater. Chem. A,* 2020, **8**, 9177-9184.
26. R.Y. Wang, B. Liu, S.J. You, Y. Li, Y. Zhang, D. Wang, B. Tang, Y.B. Sun and J.L. Zou, Three-dimensional $Ni_3Se_4$ flowers integrated with ultrathin carbon layer with strong electronic interactions for boosting oxygen reduction/evolution reactions, *Chem. Eng. J.,* 2022, **430**, 132720.
27. F.L. Lyu, Y.C. Bai, Z.W. Li, W.J. Xu, Q.F. Wang, J. Mao, L. Wang, X.W. Zhang and Y.D. Yin, Self-Templated Fabrication of CoO-$MoO_2$ Nanocages for Enhanced Oxygen Evolution, *Adv. Funct. Mater.,* 2017, **27**, 1702324.
28. J. Kim, J.N. Heo, J.Y. Do, R.K. Chava and M. Kang, Electrochemical synergies of heterostructured $Fe_2O_3$-MnO catalyst for oxygen evolution reaction in alkaline water splitting, *Nanomaterials,* 2019, **9**, 1486.
29. L. Zhao, Y.Y. Tan, Z.Y. Zhang, W. Wu, N.C. Cheng, R.Z. Ren, S.C. Mu, X.L. Sun, Defects enriched hollow porous Co-N-doped carbons embedded with ultrafine

CoFe/Co nanoparticles as bifunctional oxygen electrocatalyst for rechargeable flexible solid zinc-air batteries, *Nano Res.,* 2021, **14**, 6365-6371.
30. B. Iqbal, M. Saleem, S.N. Arshad, J. Rashid, N. Hussain and M. Zaheer, One-Pot Synthesis of Heterobimetallic Metal-Organic Frameworks (MOFs) for Multifunctional Catalysis, *Chem. Eur. J.,* 2019, **25**, 10490-10498.
31. P.C. He, Y.B. Xie, Y.B. Dou, J. Zhou, A.W. Zhou, X. Wei, J.-R. Li, Partial sulfurization of a 2D MOF array for highly efficient oxygen evolution reaction, ACS *Appl. Mater. Inter.* 2019, **11**, 41595-41601.
32. H.Y. Fang, T.Z. Huang, Y. Sun, B.T. Kang, D. Liang, S. Yao, J.M. Yu, M.M. Dinesh, S. Wu, J.Y. Lee and S. Mao, Metal-organic framework-derived core-shell-structured nitrogen-doped CoCx/FeCo@ C hybrid supported by reduced graphene oxide sheets as high performance bifunctional electrocatalysts for ORR and OER, *J. Catal.,* 2019, **371**, 185-195.
33. Y.R Huang, F.Y. Tian, Y.Q. Liu, M.G. Li, S.C. Xu, Y.S. Yu, J.M. Li, W.W. Yang, H.B. Li, Mesoporous cobalt ferrite phosphides/reduced graphene oxide as highly effective electrocatalyst for overall water splitting, *J. Colloid Interface Sci.,* 2022, **605**, 667-673.
34. P.Y. Kuang, M. He, H.Y. Zou, J.G. Yu and K. Fan, 0D/3D $MoS_2$-$NiS_2$/N-doped graphene foam composite for efficient overall water splitting, *Appl. Catal. B,* 2019, **54**, 15-25.
35. L.T. Yan, H.M. Jiang, Y. Wang, L.J. Li, X. Gu, P.C. Dai, D.D. Liu, S.-F. Tang, G.M. Zhao and K. Thomas, One-step and scalable synthesis of $Ni_2P$ nanocrystals encapsulated in N, P-codoped hierarchically porous carbon matrix using a bipyridine and phosphonate linked nickel metal-organic framework as highly efficient electrocatalysts for overall water splitting, *Electrochim. Acta,* 2019, **297**, 755-766.
36. R.H. Que, S. Liu, P. He, Y. Yang and Y.Y. Pan, Hierarchical heterostructure $CoCO_3$@NiFe LDH nanowires array as outstanding bifunctional electrocatalysts for overall water splitting, *Mater. Lett.,* 2020, **277**, 128285.
37. C.L. Chen, C. Du, D. Weng, A. Mahmood, D. Feng, J.D. Wang, Mahmood, A.; Feng, D.; Wang. J. Robust superhydrophobic polytetrafluoroethylene nanofibrous coating fabricated by self-assembly and its application for oil/water separation, ACS *Appl. Energ. Mater.,* 2018, **1**, 2632-2639.
38. X.Q. Wang, B.J. Zheng, D.X. Yang, B.C. Sun, W.L. Zhang and Y.F. Chen, Self-Assembled CoFe nanoparticle-embedded carbon nanowires as efficient nonprecious catalyst for overall water splitting, *Energy Technol.,* 2019, **7**, 1801061.
39. P.Y. Wang, J.W. Zhu, Z.H. Pu, R. Qin, C.T. Zhang, D. Chen, Q. Liu, D.L. Wu, W.Q. Li, S.L. Liu, J.S. Xiao and S.C. Mu, Interfacial engineering of Co nanoparticles/$Co_2C$ nanowires boosts overall water splitting kinetics, *Appl. Catal. B,* 2021, **296**, 120334.
40. Y.Y. Guo, P.F. Yuan, J.N. Zhang, H.C. Xia, F. Cheng, M.F. Zhou. J. Li, Y.Y. Qiao, S.C. Mu and Q. Xu, $Co_2P$-CoN Double Active Centers Confined in N-Doped Carbon Nanotube: Heterostructural Engineering for Trifunctional Catalysis toward HER, ORR, OER, and Zn-Air Batteries Driven Water Splitting, *Adv. Funct. Mater.,* 2018, **28**, 1805641.

41. H. Wang, H.J. Wang, H. Wan, D. Wu, G. Chen, N. Zhang, Y.J. Cao, X.H. Liu and R.Z. Ma, Ultrathin Nanosheet-Assembled Co-Fe Hydroxide Nanotubes: Sacrificial Template Synthesis, Topotactic Transformation, and Their Application as Electrocatalysts for Efficient Oxygen Evolution Reaction, *ACS Appl. Mater. Interfaces,* 2020, **12**, 46578-46587.
42. L.L. Huang, D.W. Chen, G. Luo, Y.-R. Lu, C. Chen, Y.Q. Zou, C.-L. Dong, Y.F. Li and S.Y. Wang, Zirconium-regulation-induced bifunctionality in 3D cobalt-iron oxide nanosheets for overall water splitting, *Adv. Mater.,* 2019, **31**, 1901439.
43. J. Shi, F. Qiu, W.B. Yuan, M.M. Guo and Z.-H. Lu, Nitrogen-doped carbon-decorated yolk-shell CoP@FeCoP micro-polyhedra derived from MOF for efficient overall water splitting, *Chem. Eng. J.,* 2021, **403**, 126312.
44. Y.C. Wu, L. Xu, W. Xin, T.T. Zhang, J.L. Cao, B.T. Liu, Q.P. Qiang, Z. Zhou, T. Han, S.X. Cao, W. Xiao and J.M. Wei, Rational construction of 3D MoNi/NiMoOx@NiFe LDH with rapid electron transfer for efficient overall water splitting, *Electrochim Acta,* 2021, **369**, 137680.
45. H. Matsushima, T. Iida and Y. Fukunaka, Observation of bubble layer formed on hydrogen and oxygen gas-evolving electrode in a magnetic field, *J Solid State Electrochem,* 2012, **16**, 617-623.
46. G. B. Darband, M. Aiofkhazraei, S. Shanmugam, Recent advances in methods and technologies for enhancing bubble detachment during electrochemical water splitting, *Rene. Sustain. Energ. Rev.,* 2019, **114**, 109300.